J|A|C|S
JOURNAL OF THE AMERICAN CHEMICAL SOCIETY

Article

pubs.acs.org/JACS

Comprehensive Experimental and Computational Analysis of Binding Energy Hot Spots at the NF-κB Essential Modulator/IKKβ Protein−Protein Interface

Mary S. Golden,[†,§] Shaun M. Cote,[†] Marianna Sayeg,[‡] Brandon S. Zerbe,[‡,∥] Elizabeth A. Villar,[†] Dmitri Beglov,[‡] Stephen L. Sazinsky,[†,⊥] Rosina M. Georgiadis,[†] Sandor Vajda,*[,†,‡] Dima Kozakov,*[,‡] and Adrian Whitty*[,†]

Departments of [†]Chemistry and [‡]Biomedical Engineering, Boston University, 590 Commonwealth Avenue, Boston, Massachusetts 02215, United States

S Supporting Information

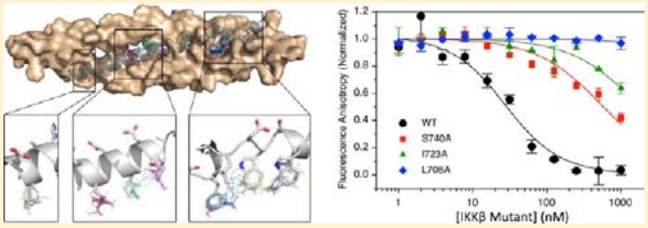

ABSTRACT: We report a comprehensive analysis of binding energy hot spots at the protein−protein interaction (PPI) interface between nuclear factor kappa B (NF-κB) essential modulator (NEMO) and IκB kinase subunit β (IKKβ), an interaction that is critical for NF-κB pathway signaling, using experimental alanine scanning mutagenesis and also the FTMap method for computational fragment screening. The experimental results confirm that the previously identified NEMO binding domain (NBD) region of IKKβ contains the highest concentration of hot-spot residues, the strongest of which are W739, W741, and L742 ($\Delta\Delta G$ = 4.3, 3.5, and 3.2 kcal/mol, respectively). The region occupied by these residues defines a potentially druggable binding site on NEMO that extends for ~16 Å to additionally include the regions that bind IKKβ L737 and F734. NBD residues D738 and S740 are also important for binding but do not make direct contact with NEMO, instead likely acting to stabilize the active conformation of surrounding residues. We additionally found two previously unknown hot-spot regions centered on IKKβ residues L708/V709 and L719/I723. The computational approach successfully identified all three hot-spot regions on IKKβ. Moreover, the method was able to accurately quantify the energetic importance of all hot-spot residues involving direct contact with NEMO. Our results provide new information to guide the discovery of small-molecule inhibitors that target the NEMO/IKKβ interaction. They additionally clarify the structural and energetic complementarity between "pocket-forming" and "pocket-occupying" hot-spot residues, and further validate computational fragment mapping as a method for identifying hot spots at PPI interfaces.

INTRODUCTION

Protein−protein interactions (PPIs) constitute a vast but largely unexploited pool of biologically compelling drug targets.[1−5] Developing inhibitors against PPI targets remains a major challenge for small-molecule drug discovery, however.[6−9] This difficulty is due primarily to the relatively flat and open topology often seen for PPI interface sites on protein surfaces. The absence of a substantial cleft or pocket of the dimensions required to accommodate a drug-sized small molecule makes it difficult to generate sufficient binding energy with a small-molecule ligand to achieve high affinity binding.[10,11] This problem is mitigated, in part, by the fact that binding energy at PPI interfaces is not distributed uniformly, but is instead concentrated into binding energy "hot spots".[12,13] The number and arrangement of hot spots is considered a key determinant of whether a given PPI interface will be "druggable" by small molecules,[14−16] and examination of a set of PPI targets for which small-molecule inhibitors exist showed that the compounds invariably interacted by binding to a cluster of strong binding energy hot spots.[17] Analysis of PPI targets to identify hot-spot locations and evaluate their strengths is therefore an important step in the structure-based discovery of PPI inhibitors, and new methods for identifying hot spots and quantifying their energetic importance are of broad interest.

Several approaches have been developed for establishing the locations and strengths of binding energy hot spots at PPI interfaces. The method of alanine scanning mutagenesis involves individually mutating interface residues to alanine, thereby eliminating side-chain atoms beyond Cβ, and then measuring the effect of each mutation on binding affinity.[18] Residues for which mutation to alanine gives a large decrease in binding energy (typically $\Delta\Delta G$ > 1.5 kcal/mol) are considered to constitute binding energy hot spots.[12] The effects of alanine mutations are not always strictly local, however, and therefore alanine scanning data cannot always be interpreted to simply reflect the amount of binding energy generated by intermolecular interactions made by the side chain in question.[19] In particular, mutation of residues that participate in forming concave binding pockets at PPI interfaces are likely

Received: January 27, 2013
Published: March 18, 2013

to give rise to nonadditive ΔΔG values, if the pocket can be disrupted by any of several different mutations.[20,21] Moreover, mutation to alanine can reduce affinity due to mechanisms unrelated to interactions at the interface, e.g., by destabilizing the unbound state of the protein or peptide or altering its conformation.[14,19] Thus, some hot spots identified by alanine scanning mutagenesis are false positives in the sense that they do not reflect energetically important binding interactions with the partner protein. Conversely, alanine scanning can miss a binding hot spot that mostly involves interaction of backbone rather than side-chain atoms. Computational approaches for simulating the results of alanine scanning mutagenesis have been reported.[22−25] A different approach to identifying binding energy hot spots instead relies on measuring or computing the extent to which different regions of a protein surface can bind small-molecule "fragment-like" probes.[26,27] Since the binding of small probes is weak, experimental screening of fragment libraries requires special techniques such as structure−activity relationships by NMR[28] or multiple solvent crystal structures (MSCS)[27,29] based on X-ray crystallography, and others.[30−33] Analysis of outcomes across a large number of experimental and computational fragment screens has established that the hit rate observed in an experimental fragment screen strongly correlates with the likelihood of identifying a high affinity drug-like ligand binding at the same site,[26] implying that the binding hot spots are characterized by their ability to bind a variety of small-molecule probes. Similar results have been obtained by virtual screening of small fragment probes, sometimes called computational fragment mapping.[34−36] For example, the FTMap algorithm places small molecular probes of various sizes and shapes on a dense grid around the protein, finds favorable positions using empirical energy functions, clusters the conformations, and ranks the clusters on the basis of the average energy.[34] The regions that bind multiple low-energy probe clusters, called consensus cluster (CC) sites, identify binding hot spots. These two functional definitions of hot spots—i.e. residues that give large ΔΔG values when mutated to alanine, versus regions on a protein surface that can interact strongly with small probes—are distinct but interrelated. In particular, we have recently shown that over 90% of side chains at PPI interfaces that are identified as hot spots by alanine scanning in fact protrude into fragment binding hot spots of the kind that are important for drug or small ligand binding.[37]

A PPI interface that is of considerable interest as a therapeutic target is that between nuclear factor kappa B (NF-κB) essential modulator (NEMO; also known as IKKγ, the gamma subunit of IκB kinase (IKK), where IκB is the inhibitor of NF-κB) and IKKβ. NEMO together with the catalytic alpha and beta subunits IKKα and IKKβ form the active IKK, which is an essential component of the canonical NF-κB signaling pathway.[38−41] NF-κB signaling is widely studied due to its involvement in critical cellular processes, including cell survival, proliferation and differentiation, and dysregulation of the pathway has been linked to a variety of inflammatory diseases and some cancers.[42−45] NF-κB signaling is activated by a wide range of stimuli, including pro-inflammatory cytokines and other receptor mediated signals. These signals lead to formation and activation of the IKK complex, which phosphorylates IκB causing it to dissociate from its latent complex with NF-κB, thereby releasing NF-κB to translocate to the nucleus where it mediates target gene transcription.[39] IKK is therefore crucial to activation of NF-κB signaling, and inhibition of IKK or disruption of the NEMO/IKKα/β interaction that holds the complex together has emerged as a promising therapeutic target.[43,44,46]

The interaction of IKKβ with NEMO has previously been studied by measuring the effects of selected point mutations of IKKβ, using a qualitative pull-down assay, and by measuring the binding activity of IKKβ-derived peptides of various lengths (Figure S1). These reports establish that NEMO interacts with the C-terminal region of IKKβ encompassing residues 701−745. Within this region residues 737−742 have been shown to comprise a critical motif for binding NEMO (Figure 1), for which reason this six residue stretch has become known as the "NEMO binding domain" (NBD).[47,48] The NBD sequence is conserved in IKKα and IKKβ, and an 11-mer IKKβ peptide encompassing the NBD was shown to block the interaction of IKKα and IKKβ with GST-NEMO in pull-down studies, and to disrupt preformed NEMO/IKKα/β complexes.[48] Truncated forms of IKKβ which lacked the NBD showed no binding to NEMO in pull-down studies.[48] NBD-containing IKKβ peptides have additionally been shown to inhibit NEMO/IKKβ binding and NF-κB signaling and function in cells and in animals.[47,49−51] Although these published studies establish the NBD as the key region of IKKβ for interacting with NEMO, the specific contributions of individual NBD residues and other IKKβ residues to NEMO binding have not been quantified. In particular, the extent to which regions of IKKβ outside of the NBD might also contribute significantly to NEMO binding has not been systematically investigated.

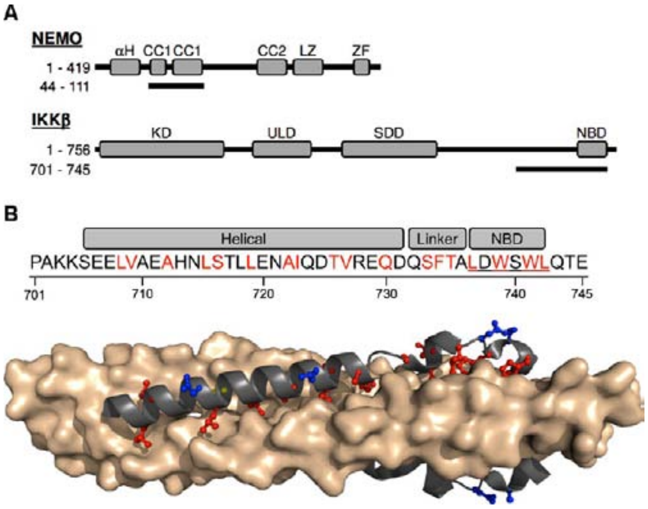

Figure 1. Interaction of NEMO with IKKβ. (A) Cartoon showing the domain structures of NEMO[52] and IKKβ.[75] The regions of NEMO and IKKβ that mediate their mutual interaction are indicated beneath each cartoon by a gray bar. (B) Structure of the NEMO(44−111) fragment (wheat) bound to a peptide derived from IKKβ residues 701−745 (gray) (PDB entry: 3BRV).[52] The sequence of the IKKβ fragment is shown at the top. IKKβ residues that make direct contact with NEMO are colored red.

An X-ray co-crystal structure is available for a peptide encompassing IKKβ residues 701−745 in complex with an N-terminal fragment (residues 44−111) of NEMO,[52] which elucidates the molecular details of the NEMO/IKKβ interaction (Figure 1B). Interestingly, the authors of this study reported that the NEMO(44−111) fragment was unstructured in the absence of IKKβ, and neither X-ray nor NMR structures are available for the relevant segment of NEMO in an unliganded state. Determining an X-ray or NMR structure for the relevant portion of NEMO without the IKKβ peptide but in the presence of fragment-sized molecules, as required to locate binding energy hot spots by experimental fragment screening, therefore appears very challenging. However, extracting the NEMO structure from the above complex, we can apply our computational fragment-based approach to identify binding hot spots on NEMO that can be useful for the design of small molecules to disrupt binding. Moreover, we have recently shown that the FTMap mapping algorithm can be extended to predict the relative changes in the binding free energy caused by mutating individual PPI interface side chains to alanine. This approach has been used in the critical assessment of predicted interactions (CAPRI) blind protein docking experiment, and gave very good results for determining how mutations in a designed protein affect its binding to influenza hemagglutinin.[53] Using an earlier version of the algorithm, which was less accurate than the one we describe in the present work, we obtained very good results in terms of the fraction of correctly labeled beneficial/neutral/deleterious mutations in the interface.[53]

Here we report a systematic analysis of energetic hot spots at the NEMO/IKKβ PPI interface, employing both experimental alanine scanning mutagenesis and FTMap computational fragment mapping. Each residue within IKKβ(701−745) that makes contact with NEMO was individually mutated to alanine, and the mutants were expressed as fusion constructs containing an engineered cleavage site to allow proteolytic removal of the fusion partner. The binding affinity of each IKKβ alanine mutant for full-length recombinant human NEMO was measured using a fluorescence anisotropy (FA) competition binding assay, allowing us to map the contribution that each contact on IKKβ makes to the overall binding affinity. In addition to quantifying the separate binding energy contributions of the individual NBD region residues, both the computational and experimental approaches identified two previously unsuspected binding energy hot spots comprising IKKβ residues Leu708/Val709 and Leu719/Ile723. Furthermore, we show that the energetic importance of each interaction derived from the computational analysis correlates strongly with the experimentally measured $\Delta\Delta G$ values. Significant deviations are found only for residues Asp738 and Ser740, which are shown to be energetically important by alanine scanning but are not predicted to be hot-spot residues by computational mapping. However, the side chains of these residues point away from the interface rather than protruding into any hot spot, demonstrating that, if no X-ray structure of the complex is available, results from alanine scanning should be used with caution for the prediction of binding hot spots with application to drug design. The combined results provide new information to guide the discovery of small-molecule inhibitors that target the NEMO/IKKβ interaction. They additionally highlight the structural and energetic relationship between "pocket-forming" and "pocket-occupying" hot-spot residues, and validate computational fragment mapping as a method for identifying hot spots at PPI interface sites.

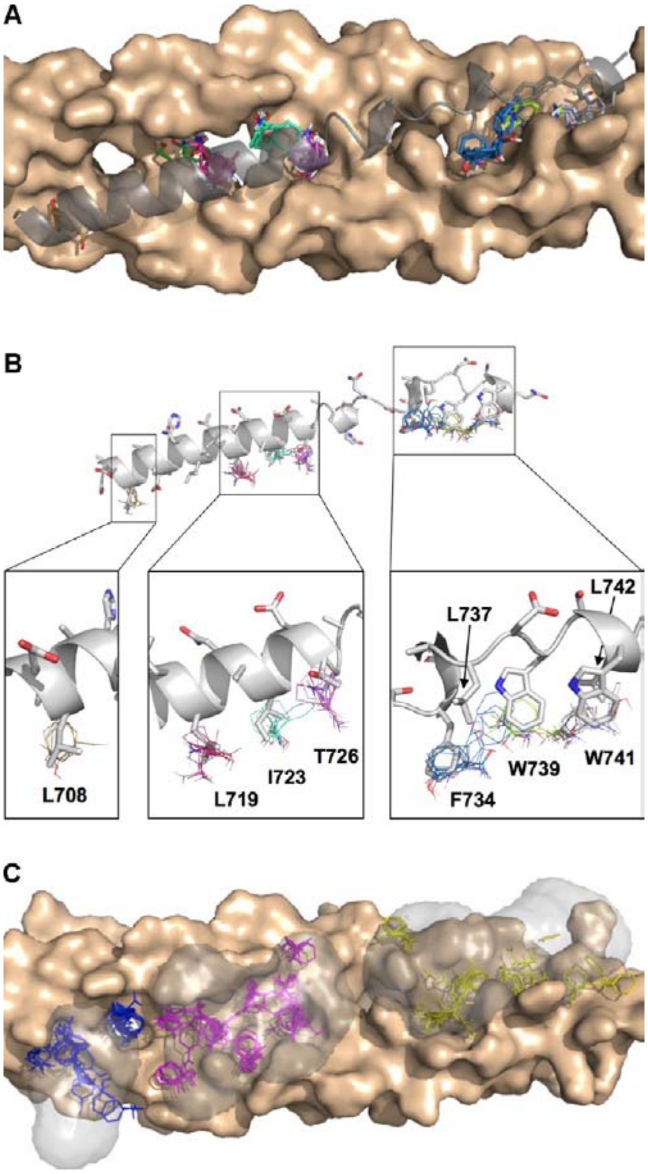

Figure 2. FTMap analysis of binding energy hot spots. (A) Results of initial global mapping analysis, showing that the observed consensus clusters define three distinct regions within the extended binding groove on NEMO. (B) Upper Panel: Results of global mapping, illustrated with the NEMO protein removed to highlight the overlap of specific IKKβ side chains with the CC sites. Lower Panels: Close-up of side-chain overlap observed in the three distinct hot-spot regions centered on IKKβ residues Phe734-Leu742 (right), Leu719-Thr726 (middle) and Leu708 (left). (C) Results of focused mapping within the search volumes (shown as transparent gray surface) surrounding each of the three hot-spot regions identified in the preliminary global mapping shown in (A). The probe clusters identified by the focused mapping are shown in yellow for the region that binds IKKβ residues Phe734-Leu742, magenta for the region binding Leu719-Thr726, and blue for the region that accommodates Leu708.

RESULTS

Computational Identification of Hot-Spot Residues on IKKβ. We first used FTMap to perform a preliminary global map of NEMO(44−111), which encompasses the entire IKKβ binding site, using the NEMO structure from the published co-crystal structure of this portion of the protein with IKKβ(701−745).[52] The results, shown in Figure 2A, identified CCs at three locations within the elongated binding groove on NEMO. The first of the three hot-spot regions (Figure 2B, right panel) is defined by the locations of CC1 (24 clusters), CC3 (18 clusters), and CC5 (16 clusters), which reside in the NEMO pockets that interact with the side chains of IKKβ residues Phe734, Leu737, Trp739, Trp741, and Leu742. The second hot spot, defined by CC2 (21 clusters), CC4 (18 clusters), and CC6 (14 clusters), includes the pockets occupied by the side chains of Leu719, Ile723, and Thr726 (Figure 2B, middle). The third hot spot includes only CC7 (7 probe clusters), located in the pocket that accommodates Leu708 of IKK*β* (Figure 2B, left). Based on this preliminary global mapping, therefore, it appears that the most important NEMO site interacts with segment 734−742 of IKK*β*, a result that agrees with the established location of the NBD region—defined as encompassing IKK*β* residues 737−742[47,48]—except that our results suggest that Phe734 also contributes to binding. Furthermore, the preliminary FTMap global analysis suggested that two additional regions of the binding groove on NEMO are also important for binding. These are centered around the sites that accommodate IKK*β* residues 719−726 and residue 708, located respectively ∼31 and ∼47 Å N-terminal of the NBD binding site.

Previous work has shown that global FTMap analysis, such as that shown in Figure 2A, correctly predicts the importance of individual sub-sites for drug and small ligand binding.[34,59,64−66] To generate results that can be directly compared with data from alanine scanning mutagenesis experiments, which reflect local rather than global binding properties at the interface, we performed additional, focused mapping at each of the three hot-spot regions identified in the preliminary global mapping. Specifically, we used the three IKK*β* sequence segments defined above to define a volume of space around each hot-spot region, and restricted the mapping probes to these regions. We did this by extending each segment by one additional amino acid at each end, and then mapping each of the three regions separately, in each case restricting the initial probe positions to the volume lying within 4 Å of any atom of the IKK*β* segment in question (Figure 2C). The focused mapping eliminated the tendency, in global mapping, for probes to be drawn away from weaker binding sites in favor of stronger sites in other regions of the protein. In addition, the focused mapping placed more probes into each region, thereby increasing the dynamic range of the mapping results. To identify which amino acids on IKK*β* comprise hot-spot residues, we used the published NEMO/IKK*β* co-crystal structure to identify all IKK*β* residues with side chains that make direct contact with NEMO, and for each we calculated the overlap density between the side-chain atoms and the FTMap probes in all nearby CCs, as described in the Experimental Section. For each position, we calculated the overlap density for the naturally occurring amino acid, and also that observed when alanine was substituted at that position. The difference in overlap density was used as a measure of the relative energetic importance of the interactions made by a given IKK*β* side chain with NEMO. The amino acids on IKK*β* that make contact with NEMO are listed in Table S1, together with the calculated difference in overlap density. The results show that IKK*β* residues W739, L719, W741, L708, I723, F734, and L742 all display a large difference in overlap density when substituted with alanine (>250 probe molecules), indicating that the side chains of these residues project into strong CCs in the binding groove on NEMO. Residues L737 and V709 show moderate levels of overlap (100−250 probe molecules), while the remainder show essentially no overlap with any CC. Mapping of the IKK*β* binding groove on the opposite face of NEMO, which has a subtly different structure presumably due to crystal packing effects, gave substantially similar results (not shown). The high overlap found for W739, W741 and other residues close to the C-terminus of IKK*β* agrees with prior reports that the region of IKK*β* extending from position 735−745 is critical for NEMO binding,[47,48] and with the prior qualitative observation that mutation of W739 or W741 to alanine resulted in loss of NEMO binding activity in a pull-down assay (Figure S1A). The double mutation S740A/L742A did not affect binding in the prior study, however, in contrast to our results which suggested that L742 is a hot-spot residue of moderate importance. In addition, the focused mapping reinforced the prediction from the preliminary global FTMap analysis that there exist two previously unsuspected binding energy hot spots, remote from the NBD region, comprising IKK*β* residues L708/V709 and L719/I723.

Experimental Alanine Scanning Mutagenesis of IKK*β*(701−745). To provide definitive experimental data on the contributions that individual contact residues on IKK*β* make to the stability of the NEMO/IKK*β* complex, we undertook a systematic alanine scan of all residues within IKK*β*(701−745) that make direct contact with NEMO. To enhance protein expression and solubility we expressed IKK*β*(701−745) fused to the C-terminus of maltose binding protein (MBP), separated by a polyasparagine (N_{10}) linker (Figure 3A). A His_6 affinity tag was appended to the C-terminus of the construct, connected by a 10-residue $(GGGGS)_2$ linker, to simplify purification, especially with respect to truncated forms of the construct in which the IKK*β*

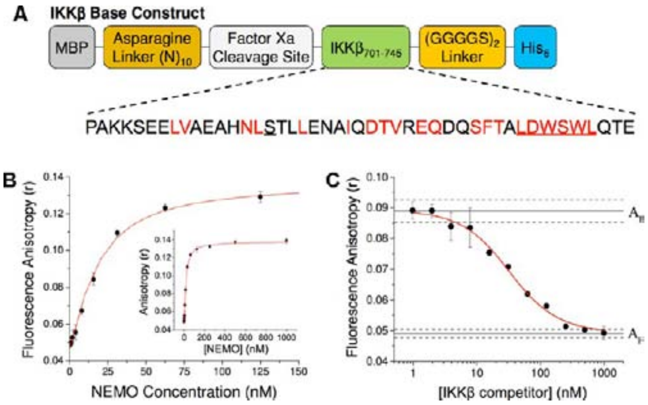

Figure 3. Structure of the MBP-IKK*β* fusion construct and development and validation of the fluorescence anisotropy binding assays. (A) Cartoon illustrating the structure of the MBP-IKK*β*-His(C716S) construct used as the base for generation of all alanine mutants used in the study. The location of the C716S mutation is underlined in black, while the previously defined NBD residues are underlined in red. Residues that were mutated to alanine in the current work are colored red. (B) Direct binding of FITC-IKK*β* to NEMO measured by FA. Error bars are the standard deviation from triplicate measurements on a single assay plate. The solid line is a fit to a quadratic binding equation, as described in the Experimental Section. Inset shows the full response curve obtained using NEMO concentrations up to 1000 nM. Data are representative of three independent experiments. (C) Concentration dependent inhibition of the binding of FITC-IKK*β* to NEMO by an unlabeled synthetic peptide comprising IKK*β*(701−745), as measured in the FA competition binding assay. Error bars represent the range of duplicate measurements from a single plate. Solid horizontal lines represent average measurements of A_B and A_F, the maximum and minimum anisotropy values of the assay, respectively. Errors in A_B and A_F values, represented as the standard deviation from triplicate measurements on a single plate, are shown as horizontal dashed lines. The solid line through the data is a fit to a competitive equilibrium binding model performed using DYNAFIT 4 software as described in the text. The data shown are representative of five independent experiments.

sequence might be absent or incomplete. We also included a Factor Xa cleavage site upstream of the IKK*β* peptide, to allow for proteolytic removal of the fusion partner if desired. Finally, we mutated IKK*β* residue Cys716 to serine, to eliminate the possibility of disulfide-linked dimerization which might affect the binding properties of the constructs. The reported NEMO/IKK*β* co-crystal structure[52] suggested that a Cys-to-Ser mutation at this site was unlikely to greatly affect binding. This final MBP-IKK*β*-His(C716S) construct, hereafter denoted as the IKK*β* "base construct", expressed well, and after purification on a Ni-NTA affinity column as described in the Experimental Section gave protein that appeared highly pure by SDS-PAGE (Figure S2). The IKK*β* base construct was characterized for NEMO binding activity as described below, and was used as the template to generate all IKK*β* mutants for the subsequent studies by site-directed mutagenesis, as described in the Experimental Section.

Validation of Fluorescence Anisotropy Binding Assay and IKKβ Constructs. To evaluate the NEMO binding activity of the IKK*β* mutants we used a FA binding assay based on competition between the unlabeled IKK*β* constructs and a fluorescein isothiocyanate (FITC)-labeled IKK*β*(701−745) synthetic peptide, FITC-IKK*β*. FA measures the change in the anisotropy of emitted fluorescence, upon excitation with plane polarized light, when a small fluorophore tumbling rapidly in solution binds to a larger and slower-tumbling receptor.[56] The less reorientation of the fluorophore that occurs within the ns lifetime of the fluorescent excited state, the more anisotropy is retained in the emitted light. Thus, if a small fluorescently labeled ligand binds to a large receptor, the emitted light shows increased anisotropy compared to the unbound ligand, and displacement of the labeled ligand by an unlabeled competitor causes a corresponding decrease in anisotropy. Note that in this study we measure FA rather than the closely related fluorescence polarization, because the change in anisotropy is directly proportional to the fraction of tracer probe bound, whereas for fluorescence polarization the relationship between these quantities is more complex.[55] Thus, while either read-out is acceptable for applications such as compound screening, FA represents the better choice when quantitative data fitting and interpretation is required.[57] Figure 3B shows that incubating a fixed concentration (15 nM) of FITC-IKK*β* with increasing concentrations of full-length recombinant NEMO gave higher anisotropy values as increasing fractions of FITC-IKK*β* became bound, with the signal saturating to a maximum value at high NEMO concentrations. The data were fitted to a standard quadratic binding equation, as described in the Experimental Section, giving a best-fit value for the binding affinity of FITC-IKK*β* for NEMO of K_{D1} = 3.6 (95% CI = 2.4−5.0) nM (n = 4), consistent with the best literature values for this interaction.[49,52,54,67] Figure 3C shows that binding of NEMO and FITC-IKK*β* (each at 15 nM final concentration) is inhibited in a dose-dependent fashion by unlabeled IKK*β*(701−745) synthetic peptide. The signal observed at maximum inhibition coincides with the minimum anisotropy value (A_F) measured in control wells containing FITC-IKK*β* but no NEMO, confirming that a sufficient concentration of the unlabeled peptide inhibitor completely blocked the binding of FITC-IKK*β*.

Analyzing inhibition curves such as that shown in Figure 3C to determine the binding affinity of the unlabeled competitor is nontrivial. The reason is that, under conditions where all three interacting components are present at concentrations close to their K_D values, the analytical equation describing the competitive equilibrium system (Scheme 1) is quite complicated, because the simplifying assumption that free concentration is approxiately equal to the total concentration cannot be made for any component.[68] The competition binding data were therefore analyzed by fitting to the competitive equilibrium binding model shown in Scheme 1, using the numerical curve-fitting software DYNAFIT 4 as described in the Experimental Section. For fitting, K_{D1} was fixed at 3.6 nM, as measured in the direct binding studies described above. For the unlabeled IKK*β* peptide shown in Figure 3C, four independent experiments gave values for K_{D2} = 14 (7.9−23) nM. This K_{D2} value is ∼4-fold higher than K_{D1} for FITC-IKK*β* measured in the direct binding assay, suggesting that the N-terminal FITC label modestly increases the binding affinity of the IKK*β* peptide.

Scheme 1. Competing Interactions Involved in the FA Competition Binding Assay[a]

$$\mathrm{NEMO{:}^{*}IKK\beta} \underset{K_{D1}}{\rightleftharpoons} \mathrm{^{*}IKK\beta + NEMO + IKK\beta_C} \underset{K_{D2}}{\rightleftharpoons} \mathrm{NEMO{:}IKK\beta_C}$$

[a] *IKK*β* represents the FITC-IKK*β* tracer probe, and IKKβ_C represents the unlabeled IKK*β* competitor. The binding affinities of FITC-IKK*β* and IKKβ_C for NEMO are designated K_{D1} and K_{D2}, respectively.

Using the competition binding assay, we also measured the binding affinities for NEMO of wild-type (WT) MBP-IKK*β*-His and for the MBP-IKK*β*-His(C716S) base construct. The results (Table 1) show that these two constructs gave binding affinities identical within experimental error to that measured for the synthetic IKK*β*(701−745) peptide. Thus, neither the presence of the MBP fusion partner and the C-terminal His tag, nor the Cys716Ser mutation, appears to significantly affect binding affinity. These results confirm that MBP-IKK*β*-His(C716S) is an appropriate construct to use as a base for the preparation of the alanine mutant set. To ensure that the results from the competition binding assay can validly be interpreted to reflect equilibrium binding, we tested the time required for binding to reach equilibrium. We did this by repeating the inhibition dose−response curves for the synthetic IKK*β* peptide, and also for the base construct, using incubation times of 1, 3, and 6 h. The results showed that measurements made at each incubation time were not significantly different (data not shown), indicating that an incubation time of 1 h is sufficient for these studies. We also tested the robustness of our

Table 1. Comparison of the Binding Affinity (K_{D2}) Measured for WT MBP-IKK*β*-His, the Base Construct, and a Synthetic IKK*β*(701-745) Peptide[a]

sample[b]	binding affinity (K_{D2}, nM)[c]
WT MBP-IKK*β*-His (n = 3)	15 (13−19)
Base Construct (n = 3)	32 (16−66)
IKK*β*(701−745) (n = 4)	14 (7.9−23)

[a] Measurements made by FA competition binding assay. [b] n is the number of independent measurements. [c] The experimental uncertainty, given in parentheses, is the 95% CI. The affinity measured for the synthetic IKK*β*(701−745) peptide was not statistically different from that measured for either WT MBP-IKK*β*-His construct ($t(5)$ = 0.117, p = 0.91) or the base construct ($t(5)$ = 1.758, p = 0.14).

data analysis with respect to experimental uncertainty in the value of K_{D1} = 3.6 nM for FITC-IKKβ, which was used as a fixed parameter in the curve fit. Competition curves for the base construct were fitted using fixed K_{D1} = 3.6, 2.4, and 5.0 nM, corresponding respectively to the lower 95% confidence interval (CI), the mean, and the upper 95% CI for this constant, and the resulting best-fit curves and K_{D2} values that were obtained were compared (Figure S6). The results show that the K_{D2} values obtained by fitting the inhibition data to the binding model shown in Scheme 1 using DYNAFIT are insensitive to small errors in K_{D1}.

Preparation and Characterization of IKKβ Alanine Mutants. Figure 3A shows the IKKβ residues selected for mutagenesis. We mutated each of the 16 IKKβ residues that are buried in the complex or appear to make some contact with NEMO at the periphery of the interface (shown in red). The set of mutants included the three NBD residues previously shown to be important for NEMO binding (Figure S1A), including D738 which does not appear to make direct contact with NEMO in the complex (Figure 1B). In addition to D738 we chose to mutate three other solvent exposed residues: these were S740, which like D738 lies in the NBD region, and also N714 and D725 which are predicted to make little contribution to binding based on their orientation away from NEMO in the X-ray crystal structure, and which were included as negative controls. In addition to the base construct, therefore, a total of 20 IKKβ variants were cloned, expressed, purified, as described in the Experimental Section, and tested for binding to NEMO in the competition binding assay. Competition binding curves were collected for each mutant and were fitted to the equilibrium binding model shown in Scheme 1, to determine the binding affinity (K_{D2}) for each mutant. Each IKKβ mutant was characterized in at least three independent experiments. Mutants were tested at final concentrations up to 1 μM; higher concentrations could not be used due to non-specific interactions with FITC-IKKβ that were seen at MBP fusion concentrations >1 μM (see the Experimental Section). Figure 4A shows representative competition data collected for a subset of IKKβ mutants illustrating the range of effects on affinity that were observed. Some IKKβ mutants showed binding affinities similar to the WT construct, indicating that the side chains of the amino acids in question do not contribute significantly to NEMO binding. However, several other mutants showed no inhibition up to a concentration of 1 μM, indicating that the mutated residues are very important for binding, while others showed intermediate behavior indicating more modest contributions.

The binding affinity values for the 20 IKKβ mutants tested, obtained from the FA competition binding studies, are collected in Table 2. The results show that the three NBD residues D738, W739, and W741 that had previously been shown to be important for NEMO binding each contributes very substantially to the stability of the complex, with mutation to alanine in each case weakening binding by K_{Rel} (= K_{D2}(Mutant)/K_{D2}(WT)) > 60, corresponding to $\Delta\Delta G$ > 2.3 kcal/mol. The adjacent residue Leu742 has a similarly large effect. Three other residues in or near the NBD region, F734, L737, and S740, also contribute substantially to binding, increasing K_{D2} by factors of K_{Rel} = 6−16, corresponding to $\Delta\Delta G$ = 1−2 kcal/mol. Outside the NBD region, our experimental results confirmed the existence of the two new binding energy hotspots in the helical portion of IKKβ that we had predicted computationally using FTMap. These are L708 ($\Delta\Delta G$ >2.3 kcal/mol), supported by V709 ($\Delta\Delta G$ = 1.7 kcal/mol), and L719 ($\Delta\Delta G$ >2.3 kcal/mol), supported by the adjacent residue from the next turn of the α-helix, I723 ($\Delta\Delta G$ = 1.9 kcal/mol). All other mutated residues, including the two solvent-exposed amino acids that were included as negative controls, showed binding affinities that were close to that of WT MBP-IKKβ-His.

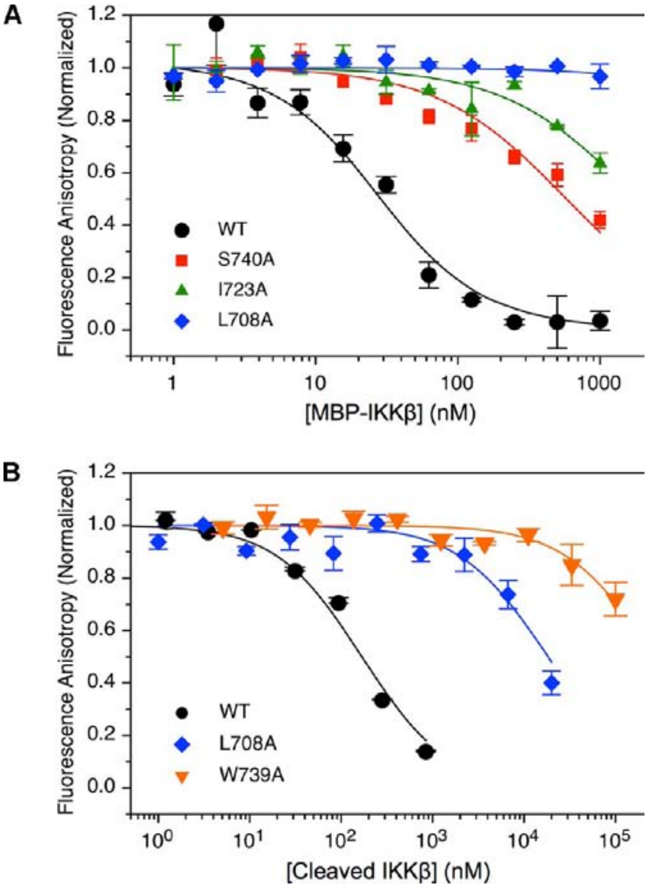

Figure 4. NEMO binding activity of IKKβ mutants. (A) FA binding data for a representative subset of MBP-IKKβ mutant constructs in the competition binding assay. (B) FA binding data for a representative subset of cleaved IKKβ mutant peptides. Anisotropy values were normalized to reflect the fractional change between the maximum observed anisotropy signal, seen at zero competitor, and the minimum observed signal, A_F, measured in the absence of NEMO. Solid lines are fits to a competitive equilibrium binding model shown in Scheme 1, using DYNAFIT 4 software. Error bars show the range of duplicate measurements. Results shown are in each case representative of at least three independent experiments.

Measurement of Highest Hot-Spot Residue Binding Energies Using Cleaved Peptides. For the six mutants, L708A, L719A, D738A, W739A, W741A, and L742A, that gave no detectable inhibition up to concentrations of 1 μM, we were able to estimate only a lower limit for K_{D2} > 870 nM, corresponding to $\Delta\Delta G$ >2.3 kcal/mol. We therefore chose these and several other mutants for more detailed analysis as cleaved peptides. The rationale for this additional step was that removing the MBP fusion partner by proteolysis with Factor Xa, taking advantage of the specific cleavage site we had engineered into the construct for this purpose, would allow us to test the IKKβ mutant peptides at higher concentrations, increasing the dynamic range of the method. The fusion constructs were therefore proteolyzed with Factor Xa, and the

Table 2. Collected Binding Affinities for MBP-IKKβ and Cleaved IKKβ Peptide Alanine Mutants

	MBP fusions		cleaved peptides		
IKKβ variant	K_{D2} (nM) (n)	95% CI	K_{D2} (nM) (n)	95% CI	K_{Rel}[a]
WT	15 (3)	13–19	24 (3)	21–29	1
L708A	$\geq 870^b$ (3)	n.a.[c]	2700 (3)	2300–3200	110
V709A	280 (4)	240–320	–[d]	–	19
N714A	3.7 (3)	3.4–4.1	–	–	0.25
L715A	8.0 (3)	6.1–11	280 (3)	160–490	0.5–12[e]
L719A	$\geq 870^b$ (3)	n.a.	21000 (3)	14000–32000	880
I723A	350 (4)	260–470	–	–	23
D725A	5.9 (3)	4.6–7.6	–	–	0.39
T726A	6.9 (3)	6.0–7.8	–	–	0.46
V727A	8.7 (3)	6.0–13	–	–	0.58
E729A	4.9 (3)	3.5–6.9	–	–	0.33
Q730A	3.9 (3)	3.1–5.1	–	–	0.26
S733A	6.2 (3)	4.5–8.5	–	–	0.41
F734A	180 (4)	120–270	–	–	12
T735A	13 (4)	9.8–18	–	–	0.87
L737A	240 (4)	130–450	–	–	16
D738A	$\geq 870^b$ (4)	n.a.	11000 (4)	9200–12000	460
W739A	$\geq 870^b$ (4)	n.a.	35000 (4)	25000–49000	1500
S740A	85 (4)	67–110	–	–	5.7
W741A	$\geq 870^b$ (3)	n.a.	9300 (3)	4300–20000	390
L742A	$\geq 870^b$ (3)	n.a.	5500 (1)	[f]	230

[a] $K_{Rel} = K_{D2}(\text{mutant})/K_{D2}(\text{WT})$. [b] Only limit was determined, because the MBP-IKKβ fusion showed ≤10% inhibition at the highest testable concentration of 1 μM (see text). [c] "n.a." = not applicable. [d] "–" = measurement with cleaved peptide was not attempted. [e] A range of values is given because for this mutant the values obtained for the MBP-IKKβ fusion and for the cleaved peptide were not in good agreement (see text). [f] No statistical uncertainty could be calculated as there was sufficient cleaved L742A peptide for only a single dose–response experiment.

resulting IKKβ peptides purified from the cleaved MBP by reversed phase HPLC, as described in the Experimental Section, and then the inhibitory potency of each peptide was characterized in the competition binding assay. In addition to the six IKKβ mutants listed above, we performed this process on the WT and C716S fusion constructs, to serve as positive controls, and on the L715A mutant that had given an anomalous dose–response curve when tested in the context of the intact fusion construct (see Experimental Section). The results are shown in Table 2. We were indeed able to test the cleaved peptides at sufficiently high concentrations to detect inhibition for even the weakest-binding of the IKKβ mutants (Figure 4B, Table 2). These experiments therefore allowed us to estimate absolute values for K_{D2} to replace the lower limits that were possible for some of the uncleaved MBP-IKKβ mutant constructs. The results (Table 2) show that the residues that contribute most to NEMO/IKKβ binding are W739 and L719 (K_{Rel} = 1500 and 880, corresponding to $\Delta\Delta G \geq 4$ kcal/mol), followed by D738, W741, and L742 ($\Delta\Delta G$ = 3–4 kcal/mol), followed by L708 ($\Delta\Delta G \approx 2.8$ kcal/mol). The curve for cleaved IKKβ L715A did not show the anomalous behavior observed for the corresponding uncleaved construct, and gave a value for K_{D2} indicating that mutation of this residue to alanine results in $\Delta\Delta G$ = 1.5 kcal/mol.

Combining the results obtained with the uncleaved MBP fusion constructs with those obtained using the cleaved peptides, as shown in Table 2, allowed us to quantify the contribution to binding energy by each of the contact residues in the NEMO binding portion of IKKβ. Figure 5A shows the $\Delta\Delta G$ values for each of the mutated residues, plotted as a histogram. These results are shown mapped onto the structure of the complex in Figure 5B. The results show that the highest concentration of hot-spot residues lies within the previously identified NBD region of IKKβ, but that two additional hot spots exist at Leu708/Val709 and Leu719/Ile723. The existence of these hot spots was not known prior to this study, but was predicted by the FTMap analysis as shown in Figure 2B.

Comparison of Experimental and Computational Measures of Hot-Spot Strength. Comparison of the results in Tables 2 and S1 show that the identities of the IKKβ residues that were predicted to be hot spots by the computational analysis agree closely with the results that were obtained experimentally. In particular, both methods identified the NBD residues L737, W739, W741, and L742 as important contributors to binding, as well as the nearby but previously untested residue F734. Moreover, the experimental results confirmed the existence of the two previously unknown hot-spot regions that the computational analysis had predicted, centered on L708/V709 and L715/I723. The only points of disagreement between the methods were for Asp738 and Ser740, which showed large effects on binding when mutated to alanine in the experimental study, but showed zero density overlap with the binding hot spots on NEMO in the FTMap analysis. This result is expected because these two residues make no contact with NEMO, instead projecting out toward solvent (Figure 1B), and thus have no overlap with any of the FTMap CCs that define the binding energy hot spots on NEMO. A quantitative comparison of the experimental and computational results is shown in Figure 5C, in which the density overlap calculated from the FTMap analysis is plotted against the experimental determined $\Delta\Delta G$ values. For those residues on IKKβ that make direct contact with NEMO the results show a strong correlation between the two data sets, with a correlation coefficient of R^2 = 0.90, indicating that ~90% of the variation in the computational prediction of hot-spot

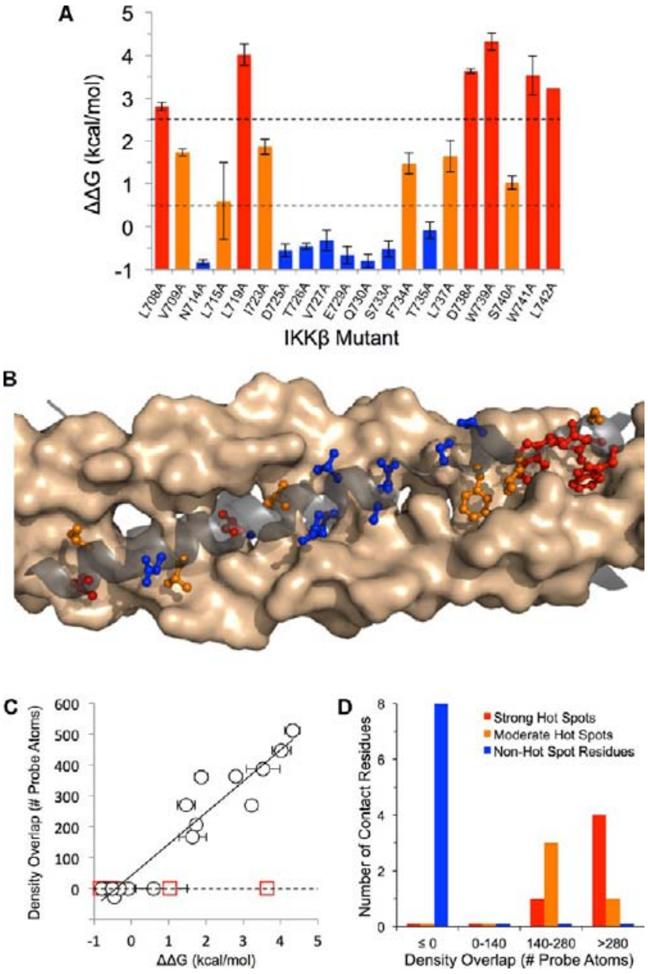

Figure 5. Hot spots determined by alanine scanning mutagenesis, and comparison to FTMap results. (A) Histogram showing the calculated contribution to NEMO/IKKβ binding energy for each amino acid mutated in the study. $\Delta\Delta G = -RT \ln(K_{D2(\text{mutant})}/K_{D2(\text{WT})})$, using the K_{D2} values shown in Table 2. The horizontal dashed lines represent cutoff thresholds indicating which $\Delta\Delta G$ values we consider to represent strong, moderate, or weak effects on NEMO binding. (B) Alanine scanning results mapped onto the structure of the NEMO/IKKβ complex.[52] Residues are color-coded as follows: red, $\Delta\Delta G > 2.5$ kcal/mol; orange, $\Delta\Delta G = 0.5-2.5$ kcal/mol; blue, $\Delta\Delta G < 0.5$ kcal/mol; gray, not tested. (C) Difference in FTMap overlap density for each mutated residue (Table S1), calculated as described in the text, plotted against the experimental $\Delta\Delta G$ values (panel A). Data for IKKβ residues that make direct contact with NEMO, as determined from the NEMO/IKKβ co-crystal structure, are plotted as circles; data for non-contact residues are plotted as squares. The solid line represents the best fit to a straight line ($R^2 = 0.90$). (D) Histogram of alanine mutants binned by the magnitude of their calculated density overlap, illustrating that, for residues that make direct contact with NEMO, the FTMap method can discriminate between strong hot spots, weak hot spots, and non-hot-spot residues.

strength can be accounted for by actual variations in the free energy of binding that were observed experimentally. Grouping the density overlap values into bins shows that the method provides excellent discrimination between strong hot spots, weaker hot spots, and non-hot-spot residues (Figure 5D). The results are robust with respect to the chosen bin size: in the current study we arbitrarily set the threshold separating strong and weak hot spots at $\Delta\Delta G = 2.5$ kcal/mol, but the plot in panel C shows that, for any other selected threshold, it would be possible to define a horizontal line across the plot (i.e., an overlap density bin size) that would provide reasonable discrimination between residues with $\Delta\Delta G$ values above and below the chosen number. Moreover, any bin size less than 167 provides complete discrimination between hot spots and non-hot-spot residues. The results in Figure 5C,D therefore suggest that the FTMap analysis is not only able to identify the locations of hot-spot residues, but also to achieve a quantitatively meaningful estimate of their relative energetic importance.

■ DISCUSSION

Alanine scanning mutagenesis is considered the definitive method for identifying energetic hot spots at PPI interfaces, for the purposes of understanding the binding energetics of particular complexes, or to identify sites at the interface that might be amenable to binding a small-molecule inhibitor. From the first, however, it has been recognized that substitution of an interface residue by alanine can reduce binding affinity by a variety of mechanisms.[19] In particular, hot-spot residues have been divided into those that form energetically important binding pockets on one binding partner, versus projecting residues on the other binding partner that protrude into those pockets.[20,37] In the current study we have performed a comprehensive alanine scan of the C-terminal region of IKKβ, which binds to a ~65 Å long groove in the N-terminal coiled-coil domain of NEMO. Elongated binding sites that accommodate extended α-helices or β-strands represent a common recognition motif among PPI complexes, including multiple examples that are of high interest as drug targets.[69−72] In our alanine scan we identified six residues on IKKβ that, when substituted by alanine, cause a reduction in binding affinity for NEMO of >2.5 kcal/mol, and a further five that weaken binding by 1.0−2.5 kcal/mol. The energetic importance of those residues in the NBD region of IKKβ mostly agrees with the qualitative results reported by May et al. (Figure S1A),[48] and we establish that among the NBD residues W739, W741, and L742 each contributes very strongly to binding, with $\Delta\Delta G$ values in the range 3.2−4.3 kcal/mol. We additionally show that L737, mutation of which did not abolish binding in the study of May et al.,[47] and F734 are also important for binding, each contributing ~1.5 kcal/mol of binding energy. These results show that the NBD binding hot spot on NEMO extends beyond the region that accommodates the previously identified six NBD residues, LDWSWL,[47,48] reaching for approximately 16 Å from the site that accommodates L742 all the way to the region that binds F734 (Figure 6). The full extent and the concentration of binding energy hot spots in this site, as revealed by our analysis, suggest that this region on NEMO represents a promising site to target with small-molecule inhibitors. A small-molecule ligand that exploits this site will presumably require an elongated structure, being either an extended acyclic molecule, or perhaps a macrocycle that binds with one edge lining the bottom of the groove. Examination of the binding geometries of the FTMap probes that define this site provides additional information to help guide inhibitor discovery. Specifically, Figure 6 shows that the probe molecules do not necessarily recapitulate the binding orientation of the IKKβ side chains that occupy this region in the complex. W739 and W741 bind with their indole rings almost parallel to each other and pointing down into the binding groove. While some FTMap probe molecules show a similar binding geometry, many probes that contain small rings

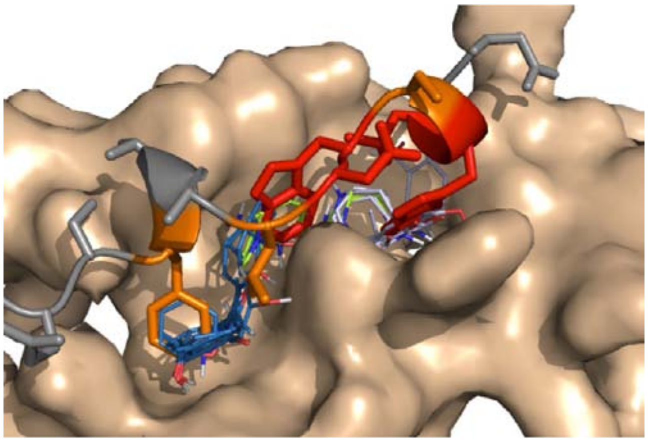

Figure 6. Close-up view of the major druggable site on NEMO. The IKKβ peptide is shown in gray, but with the strong hot-spot residues D738, W739, W741, and L742 colored red, and the moderate strength hot-spot residues F734, L737, and S740 colored orange. The FTMap probes that define the binding energy consensus sites in this region are shown as thin sticks colored blue, green, lilac, and white.

instead bind flat against the floor or lower wall of the binding groove. Similarly, some probes superimpose with the phenyl group of F734, but most adopt a perpendicular geometry (Figure 6). The probe binding geometries therefore suggest alternate ways in which this major binding site on NEMO might be filled by a small-molecule ligand, and computational approaches that search for compounds that maximize overlap with the FTMap probes might provide a useful alternative to conventional docking as a means to select compounds for experimental testing.

Our results additionally identify two new hot spots at the NEMO/IKKβ interface, centered on IKKβ residues L708/V709 and L719/I723. It has been shown previously that longer IKKβ peptides bind more strongly than short peptides that encompass just the NBD residues (Figure S1B).[49,52,67,73] Our results establish that the additional binding energy contributed by IKKβ residues upstream of the NBD region is not distributed uniformly along the binding groove, but rather is concentrated in two small regions on NEMO. Thus, the notion that PPI binding energy is focused into discrete hot spots holds true not only for the broader, flatter interfaces that have been most commonly studied by alanine scanning mutagenesis,[12,14] but also for an extended helix/strand-into-groove interface. Although the region that accommodates residues F734-L742 clearly is the primary druggable site on NEMO, these newly discovered hot spots represent additional sites that might also be exploited in drug discovery.

Among the approximately 50 IKKβ orthologues found in the Ensemble Genome Browser sequence database,[74] 37 are sufficiently homologous to the human protein in their C-terminal region that they contain a recognizable NBD sequence. An alignment of these sequences is shown in Figure S7. Among these sequences the strong NBD hot-spot residues W739, W741, and L742 are strictly conserved with the sole exception that in chicken the position of L742 is occupied by methionine. The remaining NBD contact residue, L737, is also strictly conserved despite its more modest role in binding, while F734 is frequently replaced by Leu or Met. Among the two newly identified hot spots, L719 is highly conserved, while the weaker contributing residue I723 is frequently replaced by Met, Leu, or Val. The second new hot spot shows a similar pattern: the primary residue L708 is highly conserved, except for two examples of conservative substitution to valine and in coelacanth where this position is a Glu, while the weaker companion residue V709 is substituted by Met, Ile, or Leu in ~25% of the species. Interestingly, while the hot spot comprising L719/I723 is also present in human IKKα, which binds to this same site on NEMO,[52] the hot spot at L708/V709 is not, these residues instead being replaced by Met-Ile (Figure S7). There is no crystal structure of IKKα bound to NEMO, nor have the effects on binding of mutating these IKKα residues been reported. However, to achieve strong binding IKKα, like IKKβ, presumably must generate substantial binding energy from interactions involving residues upstream of the L719/I723 hot spot. Our FTMap results suggest that the region on NEMO that accommodates L708/V709 is the only sub-site in this vicinity that is capable of generating substantial binding energy with a ligand. On this basis we would predict that the IKKα residues M708/I709 (using IKKβ sequence numbering) likely occupy this same site on NEMO, to constitute a binding energy hot spot on IKKα. If this is the case, then NEMO binding to IKKβ and IKKα would represent an example of PPIs with a common receptor in which the spatial locations of the binding energy hot spots are conserved, but alternate binding partners employ convergent solutions for how to extract binding energy by interacting at one of the hot-spot sites.

The FTMap computational method for identifying PPI hot-spot residues, a refined form of which we describe here, works on the hypothesis that the potential of a given region of a protein surface to interact with a binding partner is an intrinsic property of that site that is independent of whether the ligand is another protein or is a small molecule. Thus, a method developed to identify energetic hot spots for binding small organic molecules can be used to identify PPI hot spots by identifying residues on the protein binding partner that protrude into those sites.[37] The current study provides strong evidence that this hypothesis is correct, and further validates that such sites can be identified computationally. Moreover, we show here that this approach not only can identify the locations of binding energy hot-spot pockets that are pockets, and the complementary hot-spot residues on the binding partner that project into those pockets, but can also provide a reasonable estimate of the energetic contribution made by each projecting hot-spot residue. The ability of the method to discriminate between hot-spot and non-hot-spot residues, shown in Figure 5D, is striking, and the correlation shown in Figure 5C provides strong evidence that the overlap density provides meaningful information on the relative energetic importance of the hot spots. These findings highlight the energetic complementarity of sub-site interactions at PPI interfaces, in that the energetic importance of the hot-spot residues on IKKβ were computed solely on the basis of the energetic importance of the fragment binding sub-sites on NEMO and the degree of overlap with these sites.

IKKβ residue T726 is particularly instructive. Figure 2B shows that the atoms of this residue have extensive overlap with the probes in CC4, and yet the difference in overlap density between Thr versus Ala at this position is essentially zero. This result derives from the fact that overlap between the IKKβ atoms and the FTMap probes was calculated using hydrophobicity radii[62] rather than van der Waals radii. Alanine has a similar hydrophobicity radius to the larger but more polar threonine, resulting in comparable overlap with the FTMap probes. The experimental alanine scanning data confirms that

IKKβ derives no binding energy from interaction with Thr versus Ala at this position (Figure 5A). Indeed, the position corresponding to Thr726 is an alanine in IKKα (Figure S7). The excellent correspondence between overlap densities and measured $\Delta\Delta G$ values shown in Figure 5C, and particularly the agreement achieved for the T726A mutant, provides good validation for the use of hydrophobicity radii rather than van der Waals radii in the overlap density calculations.

Only two IKKβ residues substantially deviate from the correlation shown in Figure 4B. Asp738 had previously been identified as an important contributor to NEMO binding,[47] but the NEMO/IKKβ co-crystal structure shows that the side chain of this residue does not make direct contact with NEMO.[52] Thus, it would not be expected that FTMap would identify Asp738 as a hot-spot residue, as it is not projecting into the binding groove on NEMO and therefore can have no overlap with the FTMap probe clusters. Nevertheless, our experimental alanine scan confirmed that Asp738 is a very strong hot spot; its substitution by alanine weakens binding by ~500-fold, corresponding to a loss of binding energy of 3.6 kcal/mol that is comparable to the strongest contact hot spots on IKKβ. The large sensitivity to mutation of this non-contact residue suggests that Asp738 likely plays an important role in stabilizing the active structure of the surrounding NBD residues on IKKβ, which are not otherwise constrained into any organized secondary structure. The previous mutagenesis study of May et al. reported that, unlike substitution by alanine, mutation of Asp738 to Asn or Glu did not abolish binding to NEMO as measured in a pull-down assay.[48] These results are consistent with Asp738 exerting its structural effect through polar interactions with the side-chain and/or the amide NH of Ser740, as can be observed in the NEMO/IKKβ co-crystal structure (Figure 7). This notion is supported by the observation that alanine substitution of Ser740, which like Asp738 makes no contact with any atoms of NEMO, destabilizes binding by ~1 kcal/mol, and by the observation that IKKβ orthologues invariably contain either Asp or Glu at position 738 and either Ser or Thr at position 740. The finding that the Ser740Ala mutation generates only a fraction of the effect seen for Asp738Ala argues that interaction of the Asp738 side chain with the main-chain amide NH of Ser740 is at least as important as that with its side-chain hydroxyl group.

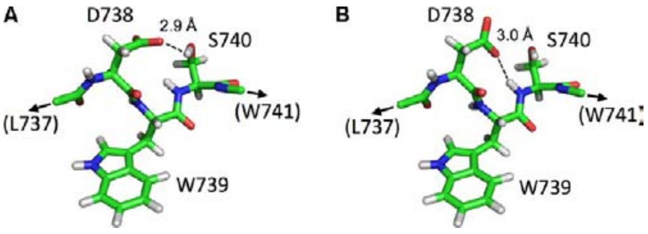

Figure 7. Details of polar interaction between Asp738 and Ser740 in the two non-identical IKKβ peptide conformations seen in the co-crystal structure of NEMO(44−111) with IKKβ(701−745).[52] (A) IKKβ peptide designated "a" in the pdb file. (B) IKKβ peptide designated "c" in the pdb file. The distances shown are the distances between the O or N atoms that are engaged in putative hydrogen-bonding interactions.

Taken together our results illustrate the existence of three distinct classes of PPI hot-spot residue at the NEMO/IKKβ binding interface: (1) residues on IKKβ that project into energetically important binding pockets, (2) residues on NEMO that form these binding pockets, and additionally (3) IKKβ residues such as Asp738 that do not themselves make significant contact at the interface, but are important for stabilizing the active conformation of nearby projecting hot-spot residues (Figure 8). Our results show that the energetic effect of this third class of hot-spot residues can be comparable to that of the strongest contact hot spots, such that absent high-resolution structural information they might be mistaken for important contact residues. To these three classes of hot-spot residue may be added a fourth, not studied in the current work, which are residues that play a structural role by indirectly stabilizing binding pockets on the concave side of the interface (Figure 8). Our results suggest that the FTMap method is effective at identifying PPI hot-spot residues that fall into classes 1 and 2, and for quantifying with reasonable precision their energetic importance, but cannot by itself directly identify hot-spot residues of classes 3 and 4. In the case of NEMO/IKKβ, and other PPI complexes that possess a helix/strand-into-groove topology, hot-spot residues from classes 2 and 4 will reside mostly on the binding partner that contains the groove, while hot-spot residues from classes 1 and 3 will reside on the binding partner that occupies this groove. However, for PPI interfaces with a flatter topology each binding partner can potentially contain hot-spot residues of all four types, depending on the local topology at different regions of the interface.

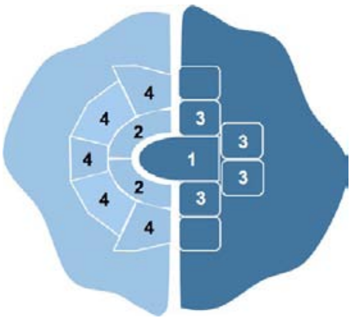

Figure 8. Illustration of distinct ways in which amino acids at or near a PPI interface can be identified as contributing to hot spots in alanine scanning mutagenesis studies. The figure shows a cartoon cross-section of a hypothetical PPI interface. The dark blue area represents a portion of one of the interacting proteins that contains a projecting hot-spot residue, labeled "1". This projecting residue binds into a pocket in the complementary surface region of the protein binding partner (light blue), which is lined by pocket-forming residues labeled "2". The residues on the first protein that are adjacent to the projecting hot-spot residue are labeled "3", and those on the second protein that help position the pocket-forming residues are labeled "4". Hot-spot residues of classes 3 and 4 may or may not themselves make direct contact with the partner protein. Mutation of any of the residues from classes 1−4 can potentially affect binding, and so might be identified as hot-spot residues in an experimental alanine scanning mutagenesis study. However, only in the case of class 1 hot-spot residues, for which the side-chain atoms are fully projecting from the protein surface, can the measured $\Delta\Delta G$ value be interpreted to reflect the binding energy that the side chain contributes to the stability of the complex. The effect on binding affinity observed upon mutation of hot-spot residues in classes 2−4 might wholly or partly reflect conformational perturbation. Our results suggest that the FTMap method described herein can identify and quantify hot-spot residues of classes 1 or 2, but not those of classes 3 and 4.

■ CONCLUSIONS

We report a comprehensive analysis of binding energy hot spots at the NEMO/IKKβ binding interface, using experimental alanine scanning mutagenesis and also an *in silico* approach based on computational fragment mapping. Our results confirm that the previously identified NBD region of IKKβ contains the highest concentration of hot-spot residues, and allowed us quantify the energetic contributions of each amino acid in this region. We also show that the most druggable binding site on NEMO extends to include the regions that bind F734 and L737. We additionally identify two new hot-spot regions on IKKβ, comprising L708/V709 and L719/I723. The FTMap computational method identified all three of these hot-spot regions on IKKβ, and was able to accurately estimate the energetic importance of all contact residues. Only in the cases of Asp738 and Ser740 did FTMap fail to correctly predict their importance for NEMO binding, because these two residues do not contact NEMO but instead exert their effects through maintaining adjacent NBD hot-spot residues in the correct orientation for binding. Taken together our results provide important information concerning potentially druggable sites on NEMO. They further establish that hot-spot residues on both the convex and concave sides of a protein–protein interface can be identified, and their energetic importance estimated, by the FTMap computational method, and clarify the different ways in which amino acid residues at protein–protein interfaces can appear to function as hot-spot residues.

■ EXPERIMENTAL SECTION

Materials. All salts, imidazole, Triton X-100, Luria broth (LB), ampicillin sodium salt, and isopropyl β-D-1-thiogalactopyranoside (IPTG) were obtained from Sigma-Aldrich (St. Louis, MO) or Fisher (Waltham, MA) and were used as received. Dithiothreitol (DTT), B-PER bacterial protein extraction reagent, lysozyme, DNase I, Gelcode Blue Safe Protein Stain, phenylmethanesulfonyl fluoride (PMSF), and HisPur Ni-NTA resin were purchased from Fisher Scientific, and Roche Complete EDTA-free protease inhibitors were obtained from Roche (Penzberg, Germany). Pfu Turbo DNA polymerase and Pfu reaction buffer, used for all polymerase chain reaction (PCR) experiments, were purchased from Stratagene/Agilent Technologies (Santa Clara, CA) along with *E. coli* BL21(DE3) competent expression cells. All restriction enzymes (*Nde*I, *Nhe*I, *Xho*I, *Nco*I, and *Dpn*I), deoxyribonucleotide triphosphates (dNTPs), Factor Xa, Quick Ligation Kit (Quick Ligase buffer and Quick Ligase), and high-efficiency *E. coli* competent cloning cells (NEB 5-alpha) were purchased from New England BioLabs (Ipswich, MA) and were used according to the manufacturer's instructions. All oligonucleotide primers used for site-directed mutagenesis of IKKβ were obtained from Integrated DNA Technologies (Coralville, IA). All samples used in these studies were prepared with ultrapure distilled water (18 MΩ·cm). Recombinant NEMO was full-length protein (residues 2–419) containing a His$_6$-tag to aid purification plus five cysteine-to-alanine substitutions, at positions 11, 76, 95, 131, and 167, which have been shown to improve the homogeneity and solubility of the protein without affecting IKKβ binding.[54] NEMO protein was expressed in *E. coli* and purified by Ni-NTA chromatography followed by gel filtration, as described.[54]

Construction of IKKβ Expression Vector. The MBP-IKKβ-His vector was made by removing DNA sequences encoding MBP, N$_{10}$, and a Factor Xa cleavage site from the cloning vector pMAL-p2x (New England BioLabs), along with a 5′ *Nde*I site and a 3′ *Nhe*I site, using standard PCR methods, and inserting them into the pET-15b vector by *Nde*I/*Nhe*I restriction enzyme digest and ligation to create a new vector, His-MBP. DNA encoding human IKKβ peptide (residues 701–745) was custom synthesized (GenScript) and inserted into the His-MBP vector. The His-MBP vector and the IKKβ peptide plasmid DNA were individually digested with *Nhe*I and *Xho*I and subsequently ligated to form the His-MBP-IKKβ vector. The His$_6$ tag was subsequently moved from the N- to the C-terminus of the construct to eliminate truncated MBP-IKKβ proteins as impurities, the His-MBP-IKKβ vector was not chosen for the mutagenesis studies. This was done by removing the region which encoded MBP to IKKβ from the His-MBP-IKKβ construct. PCR and primers that encoded a 5′ *Nco*I site and DNA for a 3′ addition of a glycine-serine linker (GGGGS)$_2$, a His$_6$-tag and a *Xho*I site were used. The resulting PCR product and the His-MBP-IKKβ vector were each digested with *Nco*I and *Xho*I and then ligated to form the new vector, MBP-IKKβ-His. All PCR procedures were performed on a MJ Mini Personal Thermal Cycler (Bio-Rad Laboratories) under the following conditions: 95 °C for 3 min, 30 cycles of 95 °C for 45 s, 55 °C for 30 s, and 72 °C for 2 min, followed by 72 °C for 10 min at the completion of the cycles, and then 4 °C until the run was manually stopped. The ligated DNA for MBP-IKKβ-His was transformed into NEB 5-alpha high-efficiency competent *E. coli* cells according to a protocol provided by the manufacturer, which were then plated onto LB-ampicillin (0.1 mg/mL) agar plates for overnight growth at 37 °C. Three colonies from each plate were inoculated into 5 mL of sterile LB containing 0.1 mg/mL ampicillin. Samples were grown overnight at 37 °C with shaking (250 rpm). The plasmid DNA was isolated using a GenCatch Plasmid DNA Miniprep Kit (Epoch Life Science Inc.) according to the manufacturer's instructions. Prior to protein expression, each expression vector was submitted for sequencing (Beckman Coulter Genomics QuickLane Express Sequencing, Phred 20 > 700). The obtained sequences were visually inspected using BioEdit Sequence Alignment Editor software (BioEdit Version 7.0.5.3) and only those with positive sequence confirmation were used.

Site-Directed Mutagenesis. All mutations were performed using standard PCR practices and the QuikChange site-directed mutagenesis kit (Agilent Technologies/Stratagene) with some modifications to the provided protocol. The base construct containing the Cys→Ser mutation (C716S) was generated using the MBP-IKKβ-His vector as the template. A forward primer (sense, s) was designed to contain at least 20 unmodified flanking base pairs on each side of the codon mutation point. Additional base pairs were added as necessary so that the sequence started and terminated with either G or C. A complementary reverse primer (anti-sense, a) was designed using online software (http://www.bioinformatics.org/sms/rev_comp.html). The DNA sequences of these primers are provided in Table S2. Stock 100 μM solutions of the forward and reverse primers were prepared in chilled distilled water and were diluted to 10 μM prior to PCR amplification. All PCR procedures were performed at a final volume of 50 μL. Template plasmid DNA, the forward and reverse primers (10 μM), dNTPs (10 mM), and Pfu Turbo (2.5 U/μL) were added at final concentrations of 1 ng/μL, 0.2 μM, 0.2 mM, and 0.05 U/μL, respectively. Pfu reaction buffer was added at a final concentration corresponding to a 10-fold dilution of the 10× stock solution. Samples were diluted to volume as necessary with chilled distilled water. PCR experiments were carried out under the following conditions: an initial denaturing step at 95 °C for 4 min, followed by 18 cycles of 95 °C for 30 s, 55 °C for 1 min, and 68 °C for 14 min. Following the last cycle the temperature was held at 4 °C until digestion of the plasmid could be performed. Methylated parental DNA was digested with Dpn I endonuclease for 2.5 h at 37 °C and then transformed into NEB 5-alpha competent *E. coli* cells. Cells were grown overnight on ampicillin selective agar plates, and the plasmid DNA was isolated and submitted for sequencing using the same procedures described for the base construct. A library of IKKβ mutants was generated using the protocols outlined above, but using the base construct (containing the C716S mutation) rather than MBP-IKKβ-His as the template vector. All primers used for the mutagenesis are included in Table S3. Twenty single-site IKKβ mutations were generated using this methodology. The sequences of all point mutation vectors were confirmed prior to protein expression.

Expression and Purification of IKKβ Mutant Fusion Proteins. The expression vector for each IKKβ mutant was transformed into *E.*

coli BL21(DE3) competent cells (Stratagene/Agilent Technologies) according to the manufacturer's instructions. The transformation solutions were plated onto LB-ampicillin (0.1 mg/mL) agar plates and incubated overnight at 37 °C. Following overnight growth, colonies were individually re-suspended in LB media containing 0.1 mg/mL ampicillin (typically 250 mL) and were grown at 37 °C with shaking (250 rpm) until an $OD_{600\ nm}$ of 0.4−0.6 was reached. Samples were then induced by the addition of 0.4 mM IPTG and were allowed to grow at 37 °C for an additional 3 h. Cells were harvested by centrifugation (5000 × *g* for 18 min) followed by overnight freezing at −80 °C. Pelleted cells were lysed by resuspension in B-PER bacterial protein extraction reagent (4 mL per gram of cell pellet) containing lysozyme (0.1 mg/mL), DNase I (5 U/mL), and Roche Complete EDTA-free protease inhibitors (1 tablet per 7 mL of extraction solution) for 15 min at room temperature. Sample lysate was clarified by centrifuging at 15000 × *g* at 4 °C for 15 min, and the supernatant was then loaded onto columns containing 1 mL of HisPur Ni-NTA resin that had been pre-equilibrated with 6 resin-bed volumes of binding buffer (25 mM sodium phosphate, 500 mM NaCl, 20 mM imidazole, pH 7.4). To avoid cross contamination, each mutant was purified on a separate column. Sample was incubated for 30 min at 4 °C after which the flow-through was collected by gravity-flow. The resin was washed with 6 column volumes of binding buffer after which protein samples were eluted by addition of 6 resin-bed volumes of elution buffer (25 mM sodium phosphate, 500 mM NaCl, 500 mM imidazole, pH 7.4). Resin was re-equilibrated with binding buffer (6 resin-bed volumes), the collected flow-through was reapplied to the column to capture protein that had not bound to the column in the first purification round, and elution was carried out as described above. Following characterization by SDS-PAGE, eluted fractions containing the protein were combined, and a buffer exchange into 10 mM HEPES, 150 mM NaCl, pH 7.4, was immediately performed using 10 000 molecular weight cutoff Amicon Ultra-15 centrifugal filters (Millipore) to avoid precipitation of the samples from prolonged storage in elution buffer. Sample concentrations were calculated from absorbance measurements taken at 280 nm using a NanoDrop 2000 spectrophotometer (Thermo Scientific) along with appropriate theoretical molar extinction coefficients calculated for each mutant (ExPASy Proteomics Server). All samples were aliquoted and frozen at −80 °C before use. All samples were >90% pure as determined by SDS-PAGE (Figure S2).

Proteolytic Cleavage and Purification of IKK*β* Mutant Peptides. IKK*β* mutant fusion proteins were treated with Factor Xa to remove the MBP fusion partner and isolate the IKK*β* peptide mutant of interest. Tests showed 1 *μ*g of Factor Xa could completely cleave 10 mg of IKK*β* mutant in 1 h at 25 °C in 10 mM HEPES, 150 mM NaCl, pH 7.4. Following cleavage, samples were treated with PMSF (final concentration 1 mM, freshly prepared from 100 mM stock solutions stored frozen in 100% isopropanol) on ice for at least 1 h. Successful cleavage of each IKK*β* mutant was confirmed by SDS-PAGE (Figure S3). Passage of the cleaved samples over a Ni/NTA affinity purification column was not successful in separating the His-tag containing IKK*β* peptide from the cleaved MPB fusion partner, because under all conditions attempted significant amounts of MBP also bound to the column and co-eluted with the cleaved IKK*β* peptide upon application of an imidazole gradient. We therefore purified each cleaved IKK*β* peptide by reversed-phase HPLC using a Resource RPC 3 mL column (GE Life Sciences), eluting with a linear gradient of 0−100% buffer B over at least 45 min (buffer A, 0.065% trifluoroacetic acid in water; buffer B, 0.05% trifluoroacetic acid in methanol). The steepness of the gradient was adjusted for each mutant to achieve baseline separation of the IKK*β* peptide from the cleaved MBP. Several HPLC purification runs were required for each mutant to obtain sufficient material for subsequent experiments. The fractions containing IKK*β* peptide from each run were pooled and lyophilized. The identity of the cleaved IKK*β* mutants was confirmed by electrospray ionization mass spectrometry.

Fluorescence Anisotropy Assays. Two FA assays were used in this work: a direct binding assay to characterize the affinity of a fluorescently labeled IKK*β* tracer peptide for NEMO (K_{D1}), and a competitive binding assay to characterize the affinity of unlabeled competitor IKK*β* derivatives for NEMO (K_{D2}). In both assays, FA measurements were performed in 96-well non-treated black polystyrene plates (Corning Costar) on a SpectraMax M5 microplate reader (Molecular Devices, Sunnyvale, CA). All buffers were equilibrated to room temperature before use. Samples were shaken on a plate shaker (UltraCruz shaker for microplates, Santa Cruz Biotechnology, Inc.) for 45 min at 300 rpm and then incubated for 15 min at 23 °C prior to anisotropy measurements. Each plate contained duplicate wells corresponding to each of 10 concentrations of competitor for the competitive binding assay, or 11 concentrations of NEMO for the direct binding studies, plus appropriate controls as described below. Each experiment was performed at least three times on separate plates. Excitation and emission wavelengths were set to 488 and 520 nm, respectively, and recorded anisotropy values were the average of 100 measurements per well. All measurements were reported in terms of FA values (*r*) rather than polarization. Anisotropy measures the intensity weighted average of bound and unbound fluorophore molecules. Therefore the fractional change in anisotropy is proportional to the percentage of bound fluorescently labeled ligand. This linear relationship does not hold for polarization measurements.[55,56] Anisotropy values are computed, using eq 1, from the

$$r = \frac{I_{\|} - I_{\perp}}{I_{\|} + 2I_{\perp}} \tag{1}$$

measured fluorescence emission intensities that are polarized parallel ($I_{\|}$) and perpendicular ($I_{\perp}$) to the plane of the incident light.[55,57]A fluorescently labeled IKK*β* tracer peptide, developed from the 45-mer IKK*β* peptide (residues 701−745) shown previously to bind specifically to NEMO,[52] was custom synthesized (Abgent, Inc.) with an N-terminal FITC label. A 45-mer IKK*β* peptide (residues 701−745), generously provided by Biogen Idec, was used as a positive control competitor. The amino acid sequences of the FITC- IKK*β* and the unlabeled control peptide are given in Table S4.

Direct binding experiments were carried out by incubating a fixed concentration of FITC-IKK*β* with various concentrations of NEMO. To wells containing two-fold serial dilutions of NEMO, 50 *μ*L each of TNT buffer (50 mM Tris-base, 200 mM NaCl, 0.01% Triton X-100, 1 mM DTT, pH 7.4, final concentration), FITC-IKK*β* (15 nM final concentration) and water were added, providing a final NEMO concentrations of ∼1−1000 nM. The intrinsic anisotropy of the unbound FITC-IKK*β* peptide (A_F), corresponding to the minimum anisotropy possible under these conditions, was measured as a negative control by omitting NEMO but including all other components at the final concentrations listed above. Data were fitted to a modified quadratic binding equation (eq 2) by nonlinear regression analysis

$$A = A_F + \frac{1}{2}R_M\{(K_{D1} + [L]_T + [R]_T) - \sqrt{(K_{D1} + [L]_T + [R]_T)^2 - 4[L]_T[R]_T}\} \tag{2}$$

using Origin curve fitting software (OriginLab Corp., Northampton, MA).In eq 2, *A* is the measured anisotropy, $[L]_T$ and $[R]_T$ are the total concentrations of ligand (FITC-IKK*β*) and receptor (NEMO), R_M is the molar response of the assay (i.e., change in anisotropy per M FITC-IKK*β*), and K_{D1} is the dissociation constant for their interaction.

Competition binding experiments were performed by incubating samples containing fixed concentrations of FITC-IKK*β* and NEMO with various concentrations of the IKK*β* competitor of interest (designated IKKβ_C). In each case, equal volumes of TNT buffer (50 mM Tris-base, 200 mM NaCl, 0.01% Triton X-100, 1 mM DTT, pH 7.4, final concentration), NEMO (9 or 15 nM final concentration), and FITC-IKK*β* (15 nM, final concentration) were added to wells containing two-fold serial dilutions of the IKK*β*-derived competitor, in 10 mM HEPES, 150 mM NaCl, pH 7.4, to give a final concentration range for competitor of ∼1−1000 nM. Reference wells were included on each assay plate to provide a measure of the maximum anisotropy signal corresponding to fully bound FITC-IKK*β* (A_B) and the minimum signal corresponding to free FITC-IKK*β* (A_F), and the results of these controls were used to evaluate the quality of each experiment and to provide parameters necessary for the fitting process. During the course of validating the FA inhibition assay four independent measurements were obtained for the binding affinity of the synthetic IKK*β*(701−745) peptide. To evaluate the binding affinity for NEMO of WT MBP-IKK*β*-His and the MBP-IKK*β* base construct (Table 1), in each case three independent replicate experiments were performed. At concentrations of MBP-IKK*β* fusion construct above 1 μM we observed an anomalous increase in FA signal. Control experiments showed that this signal resulted from nonspecific binding between the FITC-IKK*β* tracer probe and the MBP portion of the MBP-IKK*β*-His competitor when the latter was present at high concentrations. Consequently, the MBP-IKK*β*-His competitors could be tested in the FA competition binding assay only up to a concentration of 1 μM. This problem was not seen with the cleaved IKK*β* peptides, from which the MBP fusion partner had been removed by proteolysis, allowing the cleaved peptides to be tested at higher concentrations. The competition binding data were analyzed by numerical nonlinear least-squares fitting to the competitive binding mechanism shown in Scheme 1 using DYNAFIT 4 software (BioKin Ltd.).[58] In this analysis K_{D1} and A_F were fixed at their measured values, while K_{D2} and the specific molar response ($A_B - A_F$ per nanomolar FITC-IKK*β*) were obtained by fitting. Details of the fitting program are provided in the Supporting Information. The model we used to fit the inhibition data (Scheme 1) assumes that binding of IKK*β* peptides to the two opposing faces of NEMO is not cooperative, and so can be treated as independent binding events with identical K_D values. To test this assumption we attempted to fit the data using an alternative model in which the K_D values for binding of the first and second IKK*β* peptides were allowed to differ (Figure S8). The results showed that K_D values that differed substantially from each other resulted in a curve fit with a steeper slope that was incompatible with the experimental data. We therefore conclude that our use of Scheme 1 to interpret the binding data is appropriate. For the six MBP-IKK*β* mutants that showed $\leq$10% inhibition at 1 μM we used DYNAFIT to perform a simulation to establish that this result corresponds to a limiting value, $K_{D2} \geq 870$ nM (Figure S4). For both direct and competition binding measurements, values are reported as mean plus 95% CI. Confidence intervals were calculated by taking the $\log_{10}$ of the individual experimental determinations of a given K_D value and calculating the standard deviation (SD). The 95% CI limits are ±2SD, which are quoted in the text and tables after taking the antilog to convert the limits back to molar units. This treatment was used because experimental errors in measured K_D values are normally distributed around the mean on a logarithmic scale but not on a linear scale (i.e., an experimental K_D value is equally likely to be in either direction by the same factor, rather by a constant number of concentration unit, which erroneous treatment can sometimes lead to nonsensical negative values for the lower confidence limit. The fitting practices described above were appropriate for the majority of the IKK*β* mutants tested. However, the MBP fusion constructs containing L715A and V727A showed behavior that was different from the other cases. For these two mutants the level of inhibition reached an asymptote at an FA signal substantially above that observed for unbound FITC-IKK*β* alone (i.e., higher than A_F). Control experiments showed no increase in FA signal at high L715A or V727A concentrations when NEMO was absent (data not shown), ruling out nonspecific interaction with FITC-IKK*β* as a cause, and also eliminating the possibility that a contaminant in the IKK*β* mutant preparations was interfering with the assay to give a falsely high signal. Although we do not have a detailed explanation for this anomalous behavior, for the purpose of these studies when fitting the competitive binding curves for L715A and V727A the minimum anisotropy value, A_F, was allowed to vary in the curve fit to accommodate the high asymptote that was observed experimentally.

Computational Identification of Hot-Spot Residues. To identify the locations and binding strengths of hot-spot residues in the region of IKK*β* (701−745, PDB ID 3BRV chain A) that interacts with NEMO, we employed a method based on the computational fragment mapping algorithm FTMap.[34] The FTMap method identifies sites on protein surfaces that have the potential to bind small organic molecules by positioning fragment-sized small-molecule probes at a dense set of grid points close to the surface of the protein, using an empirical potential function to identify positions where the probes interact favorably, and then applying clustering and energy minimization steps to identify and rank-order the resulting binding sites. The results obtained using a set of different probe molecules are then combined to identify CC sites that bind the greatest number of probe clusters across the probe set.[34] This method has been extensively validated for its ability to identify small-molecule binding sites on conventional drug targets[34,36,59,60] and at PPI interfaces.[60] Recently we reported that the method can also identify hot spots at PPI interfaces, by showing that amino acids that have been experimentally identified by alanine scanning as hot-spot residues tend to project into the strongest CCs on the protein binding partner.[37] In the current study we introduce several refinements to the previously described FTMap method to further improve the quantitative precision and dynamic range of the results, and to predict the binding free energy changes upon mutating interface side chains to alanine. First, after identifying the hot spots by global mapping of the protein of interest, we perform separate focused mapping of each hot-spot region. Second, we calculate a probe density for each hot spot based on the results of the focused mapping. For density calculation we assign each probe atom to the grid point to which it is closest, and define the density at each grid point as the total number of the probe atoms assigned. Since the grid spacing is very small (0.8 Å), defining the density only at grid points provides an adequate measure of probe distribution. Based on this definition, the density integrated over a region of the binding site predicts the average tendency of the region for binding probes. Third, to identify which amino acids on IKK*β* comprise hot-spot residues, we identify from the published co-crystal structure all IKK*β* residues that make direct contact with NEMO, and for each we calculate the overlap with the probe density, integrating the latter over the volume occupied by the residue. In order to determine the volume of a residue we first restrict consideration to the side-chain end group as defined by Beglov et al.[61] and calculate the average of hydrophobicity volumes as defined by the Analytical Continuum Electrostatics model[62] in the CHARMM molecular modeling package.[63] The average volume is used to obtain a hydrophobicity radius. We then add 0.6 Å “padding” to this value in order to account for the fact that the probes can be located only at the grid points used in FTMap, and calculate the total volume of the residue by applying the resulting radius to the center of each atom in the residue. Our basic assumption is that the probe atom density, integrated over a residue hydrophobicity volume, is proportional to the contribution of the residue to the binding free energy. To model alanine scanning results, we also calculate the integral for an alanine residue at the same position, and determine the difference as a predictor of change in the binding free energy (i.e., the larger the loss of overlap probe density observed upon alanine substitution at a given position in IKK*β*, the more binding free energy the side chain of the residue at that position is predicted to contribute to NEMO/IKK*β* binding). Since the overlap is not normalized, the method predicts only relative contributions of individual residues, and no attempt was made to predict absolute binding free energies.

■ ASSOCIATED CONTENT

Ⓢ Supporting Information

Density overlap results for (Table S1), oligonucleotide primers used for site-directed mutagenesis (Tables S2 and S3), amino acid sequences of IKK*β* peptides used (Table S4), summary of literature data for the binding of IKK*β*-derived peptides and IKK*β* mutants to NEMO (Figure S1), SDS-PAGE data for the purified MBP-IKK*β* fusion constructs (Figure S2) and showing their subsequent proteolytic cleavage with Factor Xa (Figure S3), custom-written DYNAFIT 4 code for analyzing the competition binding data (Figure S4), simulated competition curves (Figure S5), curve-fitting robustness analysis (Figure S6), and the sequence alignment of human IKKβ(701−745) against IKKβ orthologues from 37 species and against the corresponding region of human IKKα (Figure S7). This material is available free of charge via the Internet at http://pubs.acs.org.

AUTHOR INFORMATION

Corresponding Author

whitty@bu.edu (A.W.); midas@bu.edu (D.K.); vajda@bu.edu(S.V.)

Present Addresses

§M.S.G.: Vertex Pharmaceuticals, Cambridge, MA 02139
∥B.S.Z.: Department of Human Genetics, University of California, San Francisco
⊥S.L.S.: Merrimack Pharmaceuticals, Cambridge, MA 02139

Notes

The authors declare no competing financial interest.

ACKNOWLEDGMENTS

This research was supported by NIH grants GM094551 to A.W. and S.V., GM064700 and GM61687 to S.V., and GM93147 to D.K., and by NSF grant DBI1047082 to S.V. and D.K.

REFERENCES

(1) Arkin, M. R.; Whitty, A. *Curr. Opin. Chem. Biol.* **2009**, *13*, 284.
(2) Berg, T. *Curr. Opin. Drug Discovery Dev.* **2008**, *11*, 666.
(3) Hopkins, A. L.; Groom, C. R. *Nat. Rev. Drug Discovery* **2002**, *1*, 727.
(4) Wells, J. A.; McClendon, C. L. *Nature* **2007**, *450*, 1001.
(5) Winter, A.; Higueruelo, A. P.; Marsh, M.; Sigurdardottir, A.; Pitt, W. R.; Blundell, T. L. *Q. Rev. Biophys.* **2012**, *45*, 383.
(6) Chene, P. *ChemMedChem* **2006**, *1*, 400.
(7) Domling, A. *Curr. Opin. Chem. Biol.* **2008**, *12*, 281.
(8) Makley, L. N.; Gestwicki, J. E. *Chem. Biol. Drug Des.* **2013**, *81*, 22.
(9) Zinzalla, G.; Thurston, D. E. *Future Med. Chem.* **2009**, *1*, 65.
(10) Whitty, A.; Kumaravel, G. *Nat. Chem. Biol.* **2006**, *2*, 112.
(11) Smith, M. C.; Gestwicki, J. E. *Exp. Rev. Mol. Med.* **2012**, *14*, e16.
(12) Clackson, T.; Wells, J. A. *Science* **1995**, *267*, 383.
(13) Bogan, A. A.; Thorn, K. S. *J. Mol. Biol.* **1998**, *280*, 1.
(14) DeLano, W. L. *Curr. Opin. Struct. Biol.* **2002**, *12*, 14.
(15) Moreira, I. S.; Fernandes, P. A.; Ramos, M. J. *Proteins* **2007**, *68*, 803.
(16) Ma, B.; Nussinov, R. *Curr. Top. Med. Chem.* **2007**, *7*, 999.
(17) Kozakov, D.; Hall, D. R.; Chuang, G. Y.; Cencic, R.; Brenke, R.; Grove, L. E.; Beglov, D.; Pelletier, J.; Whitty, A.; Vajda, S. *Proc. Natl. Acad. Sci. U.S.A.* **2011**, *108*, 13528.
(18) Wells, J. A. *Methods Enzymol.* **1991**, *202*, 390.
(19) Clackson, T.; Ultsch, M. H.; Wells, J. A.; de Vos, A. M. *J. Mol. Biol.* **1998**, *277*, 1111.
(20) Li, X.; Keskin, O.; Ma, B.; Nussinov, R.; Liang, J. *J. Mol. Biol.* **2004**, *344*, 781.
(21) Keskin, O.; Ma, B.; Nussinov, R. *J. Mol. Biol.* **2005**, *345*, 1281.
(22) Darnell, S. J.; Page, D.; Mitchell, J. C. *Proteins* **2007**, *68*, 813.
(23) Tuncbag, N.; Kar, G.; Keskin, O.; Gursoy, A.; Nussinov, R. *Briefings Bioinf.* **2009**, *10*, 217.
(24) Xia, J. F.; Zhao, X. M.; Song, J.; Huang, D. S. *BMC Bioinf.* **2010**, *11*, 174.
(25) Kortemme, T.; Baker, D. *Proc. Natl. Acad. Sci. U.S.A.* **2002**, *99*, 14116.
(26) Hajduk, P. J.; Huth, J. R.; Fesik, S. W. *J. Med. Chem.* **2005**, *48*, 2518.
(27) Mattos, C.; Ringe, D. *Nat. Biotechnol.* **1996**, *14*, 595.
(28) Hajduk, P. J. *Mol. Interventions* **2006**, *6*, 266.
(29) Mattos, C.; Bellamacina, C. R.; Peisach, E.; Pereira, A.; Vitkup, D.; Petsko, G. A.; Ringe, D. *J. Mol. Biol.* **2006**, *357*, 1471.
(30) de Kloe, G. E.; Retra, K.; Geitmann, M.; Kallblad, P.; Nahar, T.; van Elk, R.; Smit, A. B.; van Muijlwijk-Koezen, J. E.; Leurs, R.; Irth, H.; Danielson, U. H.; de Esch, I. J. *J. Med. Chem.* **2010**, *53*, 7192.
(31) Erlanson, D. A. *Top. Curr. Chem.* **2012**, *317*, 1.
(32) Navratilova, I.; Hopkins, A. L. *Future Med. Chem.* **2011**, 3, 1809.
(33) Scott, D. E.; Coyne, A. G.; Hudson, S. A.; Abell, C. *Biochemistry* **2012**, *51*, 4990.
(34) Brenke, R.; Kozakov, D.; Chuang, G. Y.; Beglov, D.; Hall, D.; Landon, M. R.; Mattos, C.; Vajda, S. *Bioinformatics* **2009**, *25*, 621.
(35) Dennis, S.; Kortvelyesi, T.; Vajda, S. *Proc. Natl. Acad. Sci. U.S.A.* **2002**, *99*, 4290.
(36) Landon, M. R.; Lancia, D. R., Jr.; Yu, J.; Thiel, S. C.; Vajda, S. *J. Med. Chem.* **2007**, *50*, 1231.
(37) Zerbe, B. S.; Hall, D. R.; Vajda, S.; Whitty, A.; Kozakov, D. *J. Chem. Inf. Model.* **2012**, *52*, 2236.
(38) Gautheron, J.; Courtois, G. *Cell. Mol. Life Sci.* **2010**, *67*, 3101.
(39) Gilmore, T. D. *Oncogene* **2006**, *25*, 6680.
(40) Israel, A. *Cold Spring Harbor Persp. Biol.* **2010**, *2*, a000158.
(41) Shifera, A. S. *J. Cell. Physiol.* **2010**, *223*, 558.
(42) Courtois, G.; Gilmore, T. D. *Oncogene* **2006**, *25*, 6831.
(43) Dolcet, X.; Llobet, D.; Pallares, J.; Matias-Guiu, X. *Virchows Arch.* **2005**, *446*, 475.
(44) Feinman, R.; Siegel, D. S.; Berenson, J. *Clin. Adv. Hematol. Oncol.* **2004**, *2*, 162.
(45) Salminen, A.; Huuskonen, J.; Ojala, J.; Kauppinen, A.; Kaarniranta, K.; Suuronen, T. *Ageing Res. Rev.* **2008**, *7*, 83.
(46) Ivanenkov, Y. A.; Balakin, K. V.; Lavrovsky, Y. *Mini Rev. Med. Chem.* **2011**, *11*, 55.
(47) May, M. J.; D'Acquisto, F.; Madge, L. A.; Glockner, J.; Pober, J. S.; Ghosh, S. *Science* **2000**, *289*, 1550.
(48) May, M. J.; Marienfeld, R. B.; Ghosh, S. *J. Biol. Chem.* **2002**, *277*, 45992.
(49) Baima, E. T.; Guzova, J. A.; Mathialagan, S.; Nagiec, E. E.; Hardy, M. M.; Song, L. R.; Bonar, S. L.; Weinberg, R. A.; Selness, S. R.; Woodard, S. S.; Chrencik, J.; Hood, W. F.; Schindler, J. F.; Kishore, N.; Mbalaviele, G. *J. Biol. Chem.* **2010**, *285*, 13498.
(50) Dave, S. H.; Tilstra, J. S.; Matsuoka, K.; Li, F.; Karrasch, T.; Uno, J. K.; Sepulveda, A. R.; Jobin, C.; Baldwin, A. S.; Robbins, P. D.; Plevy, S. E. *J. Immunol.* **2007**, *179*, 7852.
(51) Gaurnier-Hausser, A.; Patel, R.; Baldwin, A. S.; May, M. J.; Mason, N. J. *Clin. Cancer Res.* **2011**, *17*, 4661.
(52) Rushe, M.; Silvian, L.; Bixler, S.; Chen, L. L.; Cheung, A.; Bowes, S.; Cuervo, H.; Berkowitz, S.; Zheng, T.; Guckian, K.; Pellegrini, M.; Lugovskoy, A. *Structure* **2008**, *16*, 798.
(53) EMBL/EBI-MSD Group. CAPRI: Critical Assessment of Prediction of Interactions, http://www.ebi.ac.uk/msd-srv/capri/round26/round26.html#T55_SUMMARY_Round1.
(54) Cote, S. M.; Golden, M. S.; Gilmore, T. D.; Glover, K.; Herscovitch, M.; Ennis, T.; Whitty, A. Manuscript submitted.
(55) Lakowicz, J. R. *Principles of Fluorescence Spectroscopy*, 3rd ed.; Springer: New York, 2006.
(56) Owicki, J. C. *J. Biomol. Screen.* **2000**, *5*, 297.
(57) Roehrl, M. H. A.; Wang, J. Y.; Wagner, G. *Biochemistry* **2004**, *43*, 16056.
(58) Kuzmic, P. *Anal. Biochem.* **1996**, *237*, 260.
(59) Hall, D. R.; Ngan, C. H.; Zerbe, B. S.; Kozakov, D.; Vajda, S. *J. Chem. Inf. Model.* **2012**, *52*, 199.
(60) Kozakov, D.; Chuang, G. Y.; Beglov, D.; Vajda, S. *Trends Biochem. Sci.* **2010**, *35*, 471.
(61) Beglov, D.; Hall, D. R.; Brenke, R.; Shapovalov, M. V.; Dunbrack, R. L., Jr.; Kozakov, D.; Vajda, S. *Proteins* **2012**, *80*, 591.
(62) Schaefer, M.; Karplus, M. *J. Phys. Chem.* **1996**, *100*, 1578.
(63) Brooks, B. R.; Brooks, C. L., III; Mackerell, A. D., Jr.; Nilsson, L.; Petrella, R. J.; Roux, B.; Won, Y.; Archontis, G.; Bartels, C.; Boresch, S.; Caflisch, A.; Caves, L.; Cui, Q.; Dinner, A. R.; Feig, M.; Fischer, S.; Gao, J.; Hodoscek, M.; Im, W.; Kuczera, K.; Lazaridis, T.; Ma, J.; Ovchinnikov, V.; Paci, E.; Pastor, R. W.; Post, C. B.; Pu, J. Z.;

Schaefer, M.; Tidor, B.; Venable, R. M.; Woodcock, H. L.; Wu, X.; Yang, W.; York, D. M.; Karplus, M. *J. Comput. Chem.* **2009**, *30*, 1545.

(64) Chuang, G. Y.; Kozakov, D.; Brenke, R.; Beglov, D.; Guarnieri, F.; Vajda, S. *Biophys. J.* **2009**, *97*, 2846.

(65) Landon, M. R.; Amaro, R. E.; Baron, R.; Ngan, C. H.; Ozonoff, D.; McCammon, J. A.; Vajda, S. *Chem. Biol. Drug. Des.* **2008**, *71*, 106.

(66) Landon, M. R.; Lieberman, R. L.; Hoang, Q. Q.; Ju, S.; Caaveiro, J. M.; Orwig, S. D.; Kozakov, D.; Brenke, R.; Chuang, G. Y.; Beglov, D.; Vajda, S.; Petsko, G. A.; Ringe, D. *J. Comput. Aided Mol. Des.* **2009**, *23*, 491.

(67) Lo, Y. C.; Maddineni, U.; Chung, J. Y.; Rich, R. L.; Myszka, D. G.; Wu, H. *Biochemistry* **2008**, *47*, 3109.

(68) Hulme, E. In *Receptor-Ligand Interactions: A Practical Approach*; Hulme, E., Ed.; IRL Press at Oxford University Press: Oxford, 1992.

(69) Edwards, T. A.; Wilson, A. J. *Amino Acids* **2011**, *41*, 743.

(70) Fulda, S. *Cancer Treat. Rev.* **2012**, *38*, 760.

(71) Petros, A. M.; Huth, J. R.; Oost, T.; Park, C. M.; Ding, H.; Wang, X.; Zhang, H.; Nimmer, P.; Mendoza, R.; Sun, C.; Mack, J.; Walter, K.; Dorwin, S.; Gramling, E.; Ladror, U.; Rosenberg, S. H.; Elmore, S. W.; Fesik, S. W.; Hajduk, P. J. *Bioorg. Med. Chem. Lett.* **2010**, *20*, 6587.

(72) Shen, H.; Maki, C. G. *Curr. Pharm. Des.* **2011**, *17*, 560.

(73) Strnad, J.; McDonnell, P. A.; Riexinger, D. J.; Mapelli, C.; Cheng, L.; Gray, H.; Ryseck, R. P.; Burke, J. R. *J. Mol. Recognit.* **2006**, *19*, 227.

(74) Flicek, P.; Ahmed, I.; Amode, M. R.; Barrell, D.; Beal, K.; Brent, S.; Carvalho-Silva, D.; Clapham, P.; Coates, G.; Fairley, S.; Fitzgerald, S.; Gil, L.; Garcia-Giron, C.; Gordon, L.; Hourlier, T.; Hunt, S.; Juettemann, T.; Kahari, A. K.; Keenan, S.; Komorowska, M.; Kulesha, E.; Longden, I.; Maurel, T.; McLaren, W. M.; Muffato, M.; Nag, R.; Overduin, B.; Pignatelli, M.; Pritchard, B.; Pritchard, E.; Riat, H. S.; Ritchie, G. R.; Ruffier, M.; Schuster, M.; Sheppard, D.; Sobral, D.; Taylor, K.; Thormann, A.; Trevanion, S.; White, S.; Wilder, S. P.; Aken, B. L.; Birney, E.; Cunningham, F.; Dunham, I.; Harrow, J.; Herrero, J.; Hubbard, T. J.; Johnson, N.; Kinsella, R.; Parker, A.; Spudich, G.; Yates, A.; Zadissa, A.; Searle, S. M. *Nucleic Acids Res.* **2013**, *41*, D48.

(75) Xu, G.; Lo, Y. C.; Li, Q.; Napolitano, G.; Wu, X.; Jiang, X.; Dreano, M.; Karin, M.; Wu, H. *Nature* **2011**, *472*, 325.